VI International Conference on Particle-based Methods – Fundamentals and Applications
PARTICLES 2019
E. Oñate, M. Bischoff, D.R.J. Owen, P. Wriggers & T. Zohdi (Eds)

# VERIFICATION AND VALIDATION OF A LATTICE BOLTZMANN METHOD COUPLED WITH COMPLEX SUB-GRID SCALE TURBULENCE MODELS

**CHRISTOS GKOUDESNES[1] AND RALF DEITERDING[2]**

[1] Aerodynamics and Fluid Mechanics Research Group
Engineering and Physical Sciences Faculty
University of Southampton
Highfield Campus, Southampton SO17 1BJ, UK
e-mail: C.Gkoudesnes@soton.ac.uk, web page: http://be.linkedin.com/in/christosgkoudesnes

[2] Aerodynamics and Fluid Mechanics Research Group
Engineering and Physical Sciences Faculty
University of Southampton
Highfield Campus, Southampton SO17 1BJ, UK
e-mail: R.Deiterding@soton.ac.uk, web page: http://rdeiterding.website/

**Key words:** Lattice Boltzmann, LES, Isotropic Turbulence, Taylor Green Vortex

**Abstract.** In this paper, we present our recent work on single relaxation Lattice Boltzmann method and Large Eddy Simulation (LES) models, namely the dynamic Smagorinsky and wall-adapting local eddy-viscosity (WALE). Initially, forced and decaying homogeneous isotropic turbulence cases were run to compare direct numerical simulations with LES. Moreover, the Taylor-Green vortex was employed to further test the performance of the turbulence models under transition to turbulence. The main purpose of this work was the verification for wall-free simulations of the two newly-implemented LES models in the in-house AMROC framework.

## 1 INTRODUCTION

Two Large Eddy Simulation (LES) models, namely the Dynamic SMAgorinsky (DSMA) and the Wall-Adapting Local Eddy-viscosity (WALE), have been recently implemented in the in-house solver based on the Single Relaxation Time (SRT) Lattice Boltzmann Method (LBM) [1]. The LBM solver [2, 3, 4, 5] is part of the AMROC framework (Adaptive Mesh Refinement in Object-oriented C ++) [6]. In this paper, we verify them under wall-free circumstances by employed the test cases of Decaying Homogeneous Isotropic Turbulence (DHIT), Forced Homogeneous Isotropic Turbulence (FHIT) and Taylor-Green Vortex (TGV). For the case of FHIT, the forcing scheme of [7] was applied due to its low implementation complexity and, particularly, the ability to start a simulation with the fluid at rest. For the FHIT and TGV, the results are also compared against the Constant SMAgorinsky (CSMA) model.

## 2 LATTICE BOLTZMANN METHOD

In the standard finite difference SRT-LBM scheme the numerical step is divided into two sub-steps. The first one, called streaming, deals with exchange of information with a number of neighbour cells depending on the LBM model in use. In the current work the D3Q19 models was used. The second sub-step, namely collision, occurs locally per cell and reads

$$f_\alpha(\mathbf{x}, t+\Delta t) = \check{f}_\alpha(\mathbf{x}, t) + \frac{\Delta t}{\tau_L}(\check{f}^{eq}_\alpha(\mathbf{x}, t) - \check{f}_\alpha(\mathbf{x}, t)) + \frac{\Delta t\ w_\alpha(\mathbf{e}_\alpha \cdot \mathbf{F})}{c_s^2}. \tag{1}$$

The notation $\check{f}_\alpha$ refers to values of the distribution function after the streaming and before the collision. The equilibrium distribution function $f^{eq}_\alpha$ is truncated to second order. $\mathbf{e}_\alpha$ are the 19 lattice velocities with $w_\alpha$ the coefficients of the LBM model. $\Delta t$ is the time step, $\tau_L$ is the relaxation time and $c_s$ is the speed of sound with value $1/\sqrt{3}$. The macroscopic variables, density, velocities and pressure, can be estimated from the moments of the distribution function.

The incorporation of an LES model into AMROC-LBM is achieved through the alteration of the discrete relaxation time $\tau_L$ and its replacement by an effective discrete relaxation time $\tau^\star_L$ [8]. The difference is the addition of the eddy viscosity $\nu_t$ computed as

$$\nu_t = (C\Delta)^2 OP_{LES}, \tag{2}$$

where $C$ is a constant depending on the employed model; $\Delta$ is the spatial step size, and $OP_{LES}$ is a function expressing the characteristic timescale of each LES model.

### 2.1 The external force for FHIT

The last term in the right side of Eq. (1) is the contribution of the external force $\mathbf{F}$. In the case of the FHIT, the force of [7] was used, defined as

$$\begin{aligned} F_x &= 2\rho A\Big(\frac{\kappa_y\kappa_z}{|\kappa|^2}\Big)G(\kappa_x,\kappa_y,\kappa_z,\phi),\\ F_y &= -\rho A\Big(\frac{\kappa_x\kappa_z}{|\kappa|^2}\Big)G(\kappa_x,\kappa_y,\kappa_z,\phi),\\ F_z &= -\rho A\Big(\frac{\kappa_x\kappa_y}{|\kappa|^2}\Big)G(\kappa_x,\kappa_y,\kappa_z,\phi), \end{aligned} \tag{3}$$

where $\rho$ is the density and $A$ the acceleration with value $10^{-4}$ for all the simulations. The force was applied to the range of low wavenumbers $1 \leq \kappa_i \leq 2$, where $i \in x, y, z$ with magnitude $|\kappa|$. Finally, the phase of the force is given by the function

$$G(\kappa_x,\kappa_y,\kappa_z) = \sin\left(\frac{2\pi x}{L}\kappa_x + \frac{2\pi y}{L}\kappa_y + \frac{2\pi z}{L}\kappa_z + \phi\right), \tag{4}$$

with $\phi$ the random phase estimated by an equidistance distribution and $L$ the length of the domain which in this case was a cube with value $2\pi$.

### 2.2 CSMA

For the case of CSMA the eddy viscosity is computed as

$$\nu_t = (C_S \Delta)^2 |\overline{S}|, \tag{5}$$

where $C_S$ is a global user-defined variable and $|\overline{S}| = \sqrt{2\overline{S}_{ij}\overline{S}_{ij}}$ is the intensity of the strain rate. The notation $\overline{X}$ describes an LES filtered variable. In the LBM framework the strain rate can be computed locally per cell avoiding the use of finite differences as

$$\overline{S}_{ij} = -\frac{1}{2\rho c_s^2 \tau_L^\star} \sum_\alpha \mathbf{e}_{\alpha i}\mathbf{e}_{\alpha j}(\overline{f}_\alpha - \overline{f}_\alpha^{\,eq}). \tag{6}$$

After some algebra, $\tau_L^*$ can be also calculated locally.

### 2.3 DSMA

The implementation of the dynamic Smagorinsky in AMROC-LBM is based on the work of Premnath *et al.* [9] and follows the idea of Germano *et al.* [10], including the modification of Lilly [11]. The same formula of CSMA, Eq. (5), is also applied here for the estimation of $\nu_t$. In this case, $C$ is a local per cell variable that is computed before the streaming as

$$C^2 = -\frac{1}{2}\frac{\langle L_{ij} M_{ij} \rangle}{\langle M_{ij} M_{ij} \rangle}. \tag{7}$$

The two tensors $L_{ij}$ and $M_{ij}$ can be calculated as

$$\begin{aligned} L_{ij} &= \widehat{\overline{u}_i \overline{u}_j} - \widehat{\overline{u}}_i \widehat{\overline{u}}_j, \\ M_{ij} &= \widehat{\overline{\Delta}}^2 |\widehat{\overline{S}}| \widehat{\overline{S}}_{ij} - \overline{\Delta}^2 \widehat{|\overline{S}| \overline{S}_{ij}}, \end{aligned} \tag{8}$$

where $\widehat{\overline{x}}$ denotes a test-filtered value computed through the employment of a discrete trapezoidal filter. In Eq. (7), $\langle \cdot \rangle$ means averaging in homogeneous directions and, if the problem is statistically stationary, in time, too. In AMROC the averaging takes place locally in each cell and per time step. This has the potential of introducing local extrema with unphysical values of $C$ [11]. To alleviate this problem, $C$ is truncated as $0 \leq C \leq 0.23$. Compared to the CSMA, the application of the test-filter impose the use of central finite differences leading to non-local calculations.

### 2.4 WALE

In the WALE model a more advanced timed scale is employed to handle effectively the damping of the eddy viscosity in the vicinity of the wall [12]. The new operator is a function both of the strain rate $S_{ij}$ and the rotation rate $\Omega_{ij}$ and reads

$$OP_{WALE} = \frac{(\mathcal{J}_{ij}\mathcal{J}_{ij})^{\frac{3}{2}}}{(\overline{S}_{ij}\overline{S}_{ij})^{\frac{5}{2}} + (\mathcal{J}_{ij}\mathcal{J}_{ij})^{\frac{5}{4}}}, \tag{9}$$

where $\mathcal{J}_{ij}$ is

$$\mathcal{J}_{ij} = \overline{S}_{ik}\overline{S}_{kj} + \overline{\Omega}_{ik}\overline{\Omega}_{kj} - \frac{1}{3}\delta_{ij}(\overline{S}_{mn}\overline{S}_{mn} - \overline{\Omega}_{mn}\overline{\Omega}_{mn}). \tag{10}$$

The constant of the model $C$ is always equal to 0.5. To compute the two rates, central finite differences are used for the derivatives. Compared to DSMA, the WALE model does not need truncation corrections besides the situation where all the velocities are zero, i.e. during the initialisation of the flow field, in which scenario $\nu_t$ is set to zero.

## 3 FORCED HOMOGENEOUS ISOTROPIC TURBULENCE

The computational domain for the FHIT, DHIT and TGV test cases was a periodic cube of a $2\pi$ length. The initial conditions for the FHIT were a zero velocity field and unit density. The value of viscosity $\nu$ was used to alter for a specific resolution the value of $Re_\lambda = u'\lambda/\nu$, where $u'$ is the root mean square of the velocity and $\lambda$ the Taylor length scale. After a transient time $\Delta t_t$, the external energy due to the force equilibrates with the viscous dissipation and a statistically steady state is achieved for a duration of $\Delta t_a$. The library FFTW [13] was employed to perform the essential Fourier transforms. The end of the transient time was decided by examining the evolution of the kinetic energy $k$ and particularly the dissipation rate $\varepsilon$. Figure 1 presents an example of their evolution for a specific simulation. The time has been normalised by the eddy turnover time $\tau_e = L_{11}/u'$, where $L_{11}$ is the integral length scale.

Initially, Direct Numerical Simulations (DNS) for a variety of resolutions and viscosity value equals to $5 \cdot 10^{-5}$ were simulated to validate the LBM solver. As a benchmark, the model spectrum of [14] has been used. Simultaneously, the performance of the applied force to be used as a verification tool was evaluated. Table 1 shows some parameters and the measured statistics of four simulations with different resolutions. In this table, we also report the Kolmogorov scales, $\eta$ the Kolmogorov length scale, $u_\eta$ the Kolmogorov velocity scale and $\tau_\eta$ the Kolmogorov time scale. For more information on the computation of the mentioned turbulent statistics the interested reader can refer to [14].

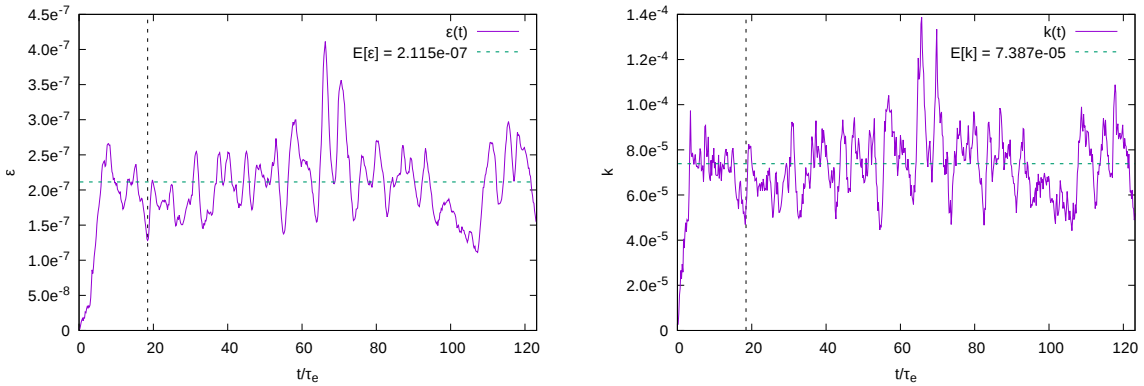


Figure 1: Time evolution of dissipation rate $\varepsilon$ (left) and turbulent kinetic energy $k$ (right) for DNS of resolution of $128^3$ cells and $\nu = 5 \cdot 10^{-5}$. The vertical dashed line shows the onset of the averaging time. The horizontal dashed line is the averaged value.

Table 1: Turbulent statistics and simulation parameters for LBM DNS for the FHIT case.

| $N^3$ | $32^3$ | $128^3$ | $256^3$ | $512^3$ |
|---|---|---|---|---|
| $\Delta t$ | 2 x $10^{-1}$ | 4.9 x $10^{-2}$ | 2.5 x $10^{-2}$ | 1.2 x $10^{-2}$ |
| $Re_\lambda$ | 47 | 59 | 66 | 69 |
| $k$ | 2.6 x $10^{-5}$ | 7.4 x $10^{-5}$ | 1.2 x $10^{-4}$ | 1.5 x $10^{-4}$ |
| $\varepsilon$ | 4 x $10^{-8}$ | 2.1 x $10^{-7}$ | 4.3 x $10^{-7}$ | 6.2 x $10^{-7}$ |
| $\kappa_{max}\eta$ | 6.8 x $10^{-1}$ | 1.8 | 3 | 5.4 |
| $\eta$ | 4.2 x $10^{-2}$ | 2.8 x $10^{-2}$ | 2.3 x $10^{-2}$ | 2.1 x $10^{-2}$ |
| $\lambda$ | 5.7 x $10^{-1}$ | 4.2 x $10^{-1}$ | 3.7 x $10^{-1}$ | 3.5 x $10^{-1}$ |
| $L_{11}$ | 1 | 9.3 x $10^{-1}$ | 9 x $10^{-1}$ | 8.8 x $10^{-1}$ |
| $L(= k^{3/2}/\varepsilon)$ | 3.2 | 3 | 3 | 2.9 |
| $u_\eta$ | 1.2 x $10^{-3}$ | 1.8 x $10^{-3}$ | 2.1 x $10^{-3}$ | 2.4 x $10^{-3}$ |
| $u'$ | 4.1 x $10^{-3}$ | 7 x $10^{-3}$ | 8.9 x $10^{-3}$ | 9.9 x $10^{-3}$ |
| $\tau_\eta$ | 35.9 | 15.7 | 11 | 9 |
| $k/\varepsilon$ | 632.1 | 349.3 | 274.4 | 238.9 |
| $\tau_e$ | 250.51 | 132.94 | 101.6 | 88.5 |
| $\Delta t_a/\tau_e$ | 63.88 | 104.68 | 68.5 | 19.1 |
| $\Delta t_t/\tau_e$ | 15.68 | 18.46 | 12.08 | 8.32 |

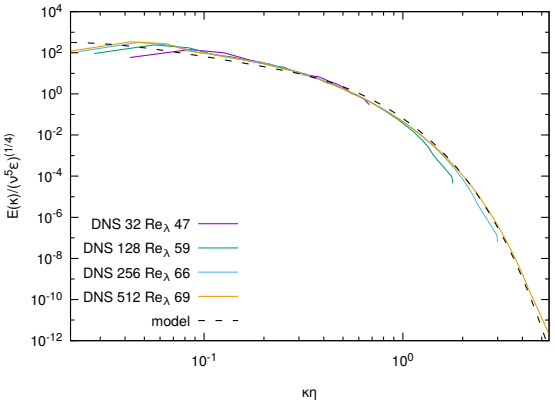


Figure 2: Time-averaged Kolmogorov energy spectra of LBM DNS for four resolutions (solid) and the model spectrum (dashed) [14] for $\nu = 5 \cdot 10^{-5}$.

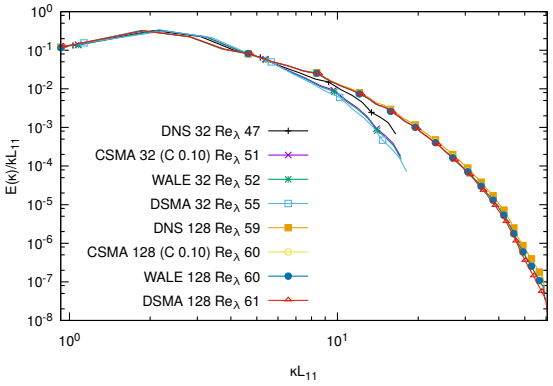


Figure 3: Time-averaged energy spectra normalised by $k$ and $L_{11}$ of LBM DNS and LES for two resolutions and a value of $\nu = 5 \cdot 10^{-5}$.

Comparing the turbulent statistics in Table 1, it is evident that there is a resolution dependence for the input energy due to the current forcing scheme affecting the other turbulent statistics, too. However, by applying Kolmogorov normalisation for the spectra, it is possible to compare them, as one can see in Fig. 2. Due to the different $Re_\lambda$ per resolution the spectra do not collapse in the lower wavenumbers. On the other hand, it is the numerical dissipation that prevents the spectra from aligning with the model one, besides the highest resolution of $512^3$ cells or $\kappa_{max}\eta > 5$.

The results and particularly the energy spectra of DNS have validated the AMROC-LBM solver to deal with elementary turbulent flows. Moreover, this DNS database was used for comparison for the verification of the LES models. Table 2 shows the measured

Table 2: Turbulent statistics and simulation parameters for LBM LES simulations for two resolutions of the FHIT test case.

| | CSMA ($C = 0.1$) | | DSMA | | WALE | |
|---|---|---|---|---|---|---|
| $N^3$ | $32^3$ | $128^3$ | $32^3$ | $128^3$ | $32^3$ | $128^3$ |
| $\Delta t$ | 2 x $10^{-1}$ | 4.9 x $10^{-2}$ | 2 x $10^{-1}$ | 4.9 x $10^{-2}$ | 2 x $10^{-1}$ | 4.9 x $10^{-2}$ |
| $Re_\lambda$ | 51 | 60 | 55 | 61 | 52 | 60 |
| $k$ | 2.5 x $10^{-5}$ | 7.3 x $10^{-5}$ | 2.5 x $10^{-5}$ | 7.3 x $10^{-5}$ | 2.5 x $10^{-5}$ | 7.4 x $10^{-5}$ |
| $\varepsilon$ | 3.1 x $10^{-8}$ | 2 x $10^{-7}$ | 2.7 x $10^{-8}$ | 1.9 x $10^{-7}$ | 3 x $10^{-8}$ | 2 x $10^{-7}$ |
| $\kappa_{max}\eta$ | 7.2 x $10^{-1}$ | 1.8 | 7.5 x $10^{-1}$ | 1.8 | 7.3 x $10^{-1}$ | 1.8 |
| $\eta$ | 4.5 x $10^{-2}$ | 2.8 x $10^{-2}$ | 4.7 x $10^{-2}$ | 2.9 x $10^{-2}$ | 4.5 x $10^{-2}$ | 2.8 x $10^{-2}$ |
| $\lambda$ | 6.3 x $10^{-1}$ | 4.3 x $10^{-1}$ | 6.8 x $10^{-1}$ | 4.4 x $10^{-1}$ | 6.4 x $10^{-1}$ | 4.3 x $10^{-1}$ |
| $L_{11}$ | 1.08 | 9.3 x $10^{-1}$ | 1.13 | 9.5 x $10^{-1}$ | 1.08 | 9.3 x $10^{-1}$ |
| $L$ | 4 | 3.1 | 4.6 | 3.3 | 4.1 | 3.2 |
| $u_\eta$ | 1.1 x $10^{-3}$ | 1.8 x $10^{-3}$ | 1.1 x $10^{-3}$ | 1.8 x $10^{-3}$ | 1.1 x $10^{-3}$ | 1.8 x $10^{-3}$ |
| $u'$ | 4.1 x $10^{-3}$ | 7 x $10^{-3}$ | 4 x $10^{-3}$ | 7 x $10^{-3}$ | 4.1 x $10^{-3}$ | 7 x $10^{-3}$ |
| $\tau_\eta$ | 40.4 | 16.1 | 44 | 16.4 | 41.3 | 16.1 |
| $k/\varepsilon$ | 796.1 | 363.6 | 928.8 | 380.8 | 823 | 367.7 |
| $\tau_e$ | 264.47 | 133.47 | 280.63 | 136.29 | 267.14 | 133.18 |
| $\Delta t_a/\tau_e$ | 60.51 | 113.09 | 57.02 | 98.15 | 59.9 | 100.44 |
| $\Delta t_t/\tau_e$ | 14.8 | 9.19 | 14 | 21.61 | 14.7 | 22.11 |

statistics of LBM LES for two resolutions, namely $32^3$ and $128^3$ cells. To assist the discussion, Fig. 3 presents the energy spectra of the LES models and DNS for this two resolutions. The spectra are normalised by the turbulent kinetic energy $k$ and the integral length scale $L_{11}$. Under this normalisation the spectra should collapse in the energy-containing range, which is verified by the plot. The lowest resolution is under-resolved based on the previous data, $\kappa_{max}\eta = 0.68$, while the other one is well-resolved, $\kappa_{max}\eta = 1.8$. Therefore, we can examine the behaviour of the LES models for both scenarios.

First of all, in the case of the well-resolved resolution, the spectra of all three LES models have collapsed to the one of DNS. This behaviour can be also identified by comparing Table 1 and Table 2 for the resolution of $128^3$ cells. The turbulent statistics are identical for all simulations. This indicates the shut-down of the LES models in well-resolved meshes as it is expected.

On the other hand, for the lowest resolution, all LES models have diverged for the DNS spectrum in the higher wavenumbers, showing increased dissipation in this range. In this way, by reducing the energy of the small scales, the turbulence models stabilise the simulation. Indeed, all three LES models have estimated higher values of $\kappa_{max}\eta$ compared to their DNS counterpart. This behaviour is highly important for running high $Re$ number flows with a low dissipation scheme such as the SRT-LBM. Moreover, by further examining the data, the CSMA with $C = 0.1$ had identical results as the WALE. Considering the isotropy of this test case, this was expected. On the contrary, the DSMA returned the highest value of $\kappa_{max}\eta$ with the smallest estimated dissipation rate $\varepsilon$. These results indicate increased values of eddy viscosity compared to the other models and thus a more dissipative behaviour.

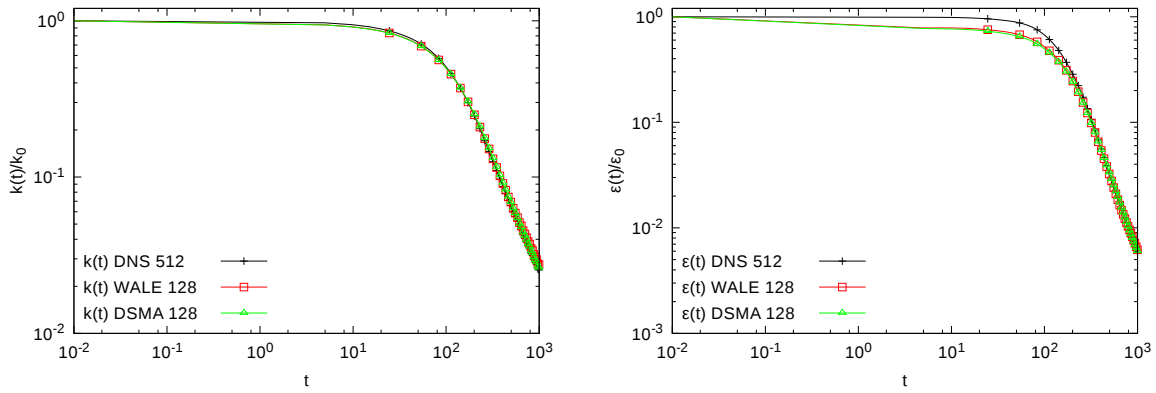


Figure 4: Evolution of the turbulent kinetic energy $k$ (left) and dissipation rate $\varepsilon$ (right) for DNS of $512^3$ against DSMA and WALE of $128^3$ cells resolution.

## 4 DECAYING HOMOGENEOUS ISOTROPIC TURBULENCE

To further exploit the above mentioned set-up, we restarted the DNS simulation of $512^3$ resolution from the final saved time step without the forcing scheme. Simultaneously, by appropriately locally volume-averaging the same initial data, we run DSMA and WALE simulations of a resolution of $128^3$ cells, again without the employment of the force. Under this set-up, one can examine DHIT. We have also tried to initialise a DNS of $128^3$ cells using the same procedure but it crashed.

Figure 4 shows the evolution of the turbulent kinetic energy $k$ and the dissipation rate $\varepsilon$ for the three simulations. Their initial values have been used to normalise both variables. All simulations were run for 1000 time units. It is evident that all three simulations have estimated similar behaviour for the evolution of the turbulent kinetic energy $k$. On the other hand, the LES models have deviated from the DNS solution in the case of the dissipation rate $\varepsilon$ for the first 300 time units. However, after this initial period, their solution collapsed with the DNS data. At this point, it is important to mention that we have not experienced the deviations reported in [15], where the DSMA model of $32^3$ cells resolution was compared against DNS of $64^3$ for a similar case. Moreover, another vital difference is that the Multi Relaxation Time (MRT) collision model was used instead of the SRT in our case.

To further evaluate the LES models, Fig. 5 shows the energy spectra for the three models after 100 and 1400 iterations, at $t = 4.91$ and $t = 68.72$, respectively. Both of these times lie in the initial period of the deviation in the dissipation rate $\varepsilon$. It is clear that the spectra in both times collapse in the energy-containing range and they only deviate in higher wavenumbers due to the lower resolution and the application of the filtering due to LES. We have also plotted the spectra at $t = 1000$ (not shown here), and the situation was identical. This is a strong indication of the expected behaviour of the implemented models.

Finally, Fig. 6 shows the vorticity field of the three models for the two previously mentioned times. First of all, both LES models have predicted similar flow fields. On

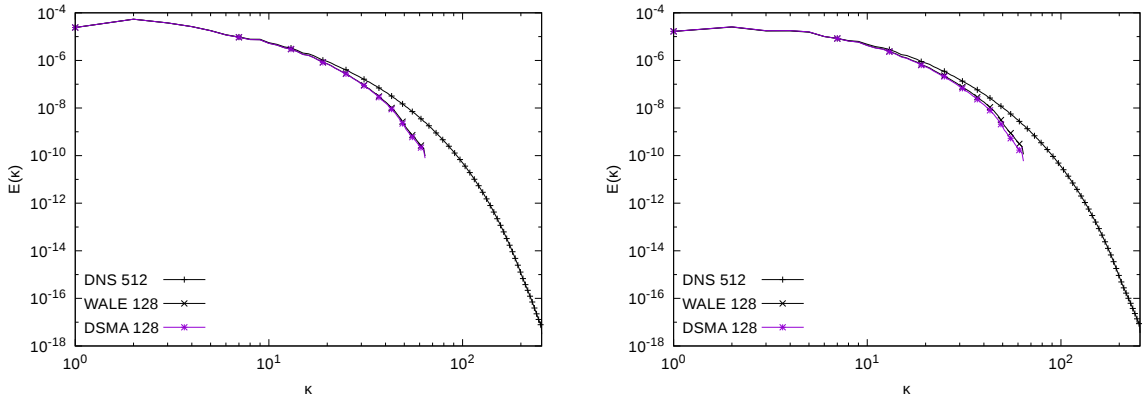


Figure 5: Energy spectra at $t = 4.91$ (left) and at $t = 68.72$ (right) for DNS of $512^3$ against DSMA and WALE of $128^3$ cells resolution.

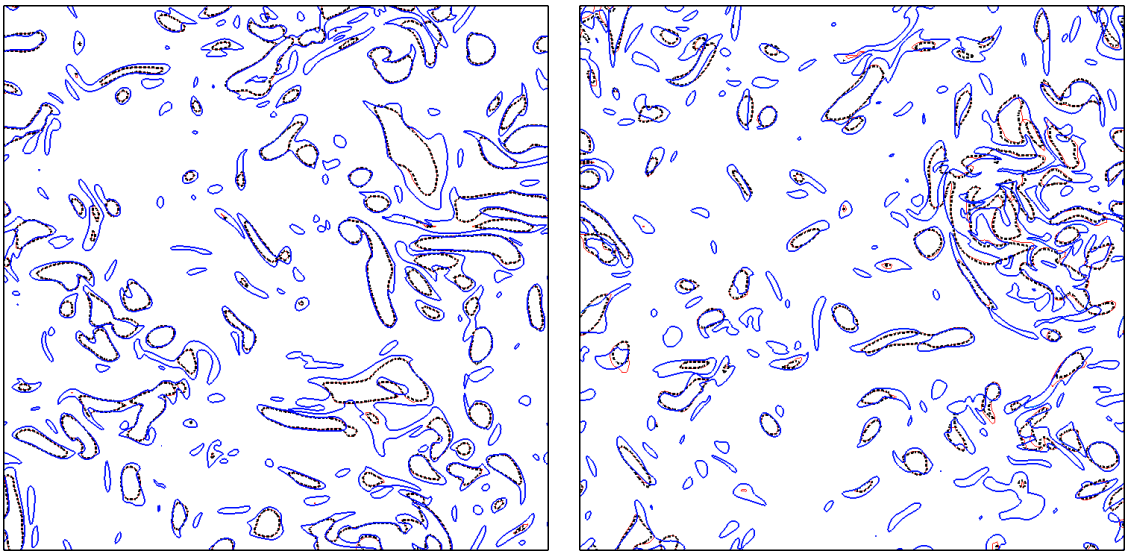

Figure 6: Contours of vorticity magnitude ($|\omega| = 0.18$) at $t = 4.91$ (left) and $t = 68.72$ (right) for DNS (thin blue lines) of $512^3$ against DSMA (dotted black lines) and WALE (thick red lines) of $128^3$ cells resolution.

the other hand, the DNS solution of the higher resolution has captured much finer scales. However, the LES models were able to simulate the majority of large eddies appearing in the DNS.

## 5 TAYLOR GREEN VORTEX

The TGV case was chosen as the final wall-free benchmark for the newly implemented LES models. Again the domain was a periodic cube with a length equal to $2\pi L$, where $L = 1$. There is no external force, while the initial conditions read

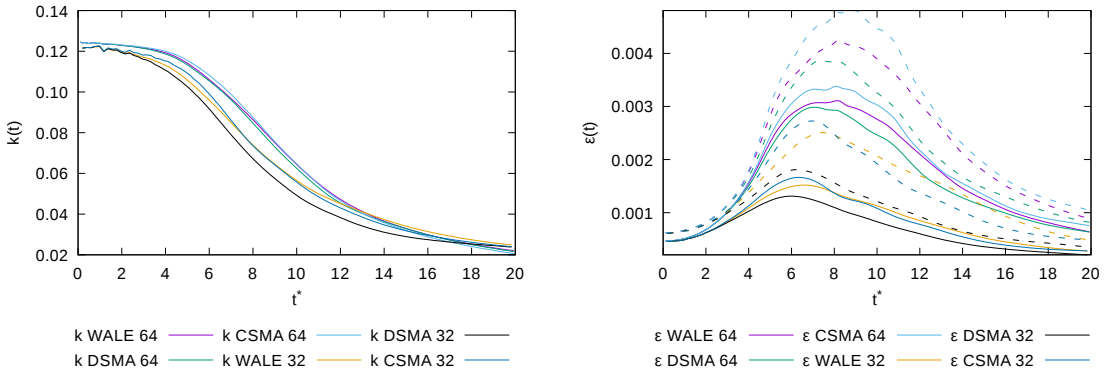


Figure 7: Evolution of kinetic energy (left) and kinetic energy dissipation rate (dashed) against dissipation rate based on enstrophy (solid) (right) of LES for two resolutions.

$$u(\mathbf{x},t_0) = U_0 \sin\left(\frac{x}{L}\right)\cos\left(\frac{y}{L}\right)\cos\left(\frac{z}{L}\right), \quad v(\mathbf{x},t_0) = -U_0\cos\left(\frac{x}{L}\right)\sin\left(\frac{y}{L}\right)\cos\left(\frac{z}{L}\right),$$
$$w(\mathbf{x},t_0) = 0, \qquad \rho(\mathbf{x},t_0) = \rho_0 + \frac{\rho_0 U_0^2}{16c_s^2}\left[\cos\left(\frac{2x}{L}\right)+\cos\left(\frac{2y}{L}\right)\right]\left[\cos\left(\frac{2z}{L}\right)+2\right]. \quad (11)$$

In the above, $\rho_0 = 1$ and $U_0 = 0.1$ leading to Ma $\approx 0.17$. To achieve $\mathrm{Re} = U_0 L/\nu = 1600$, the viscosity $\nu$ was set to $6.25 \cdot 10^{-5}$. Due to the imposed initial conditions, large scale vortices appear initially in the flowfield. As the time passes, they will start to break into smaller eddies that finally will be dissipated. Therefore, this test case has an initial inviscid part that is followed by transition to turbulence and finishes with the decay of turbulence. The above procedure imposes new challenges for the new models.

To test them, two resolutions of $32^3$ and $64^3$ cells were simulated for WALE, DSMA and CSMA, with $C = 0.1$, while their DNS counterparts crashed. The left plot in Fig. 7 shows the evolution of the turbulent kinetic energy $k$ for these simulations. Firstly, for the lowest resolution some oscillations can be detected in the initial part for all three models indicating insufficient number of cells. For $t^* > 3$, the lines predicted by the three models are diverged, with DSMA has the largest diversion. On the contrary, the WALE is able to recover and for $t^* > 7$ returns similar values to CSMA. This diversion indicates that both WALE and, particularly, DSMA have added extra dissipation during the transition phase compared to CSMA, with $C = 0.1$. The extra dissipation has led to the appearance of fewer small eddies and thus reduction in the peak of the kinetic energy dissipation rate, as one can see in the right plot of Fig. 7. The WALE has predicted a lower peak compared to CSMA. However, it has a smoother slope for the rest of the time showing that was able to adjust better during the phase of decay of turbulence. Moreover, in this plot, the difference between the two dissipations is a measure of the numerical dissipation. In that respect, DSMA had the best performance.

For the highest resolution, there are no apparent discrepancies in the evolution of the turbulent kinetic energy $k$ for the three models. Examining the evolution of the dissipation rates, again both WALE and DSMA have exaggerated the dissipation during

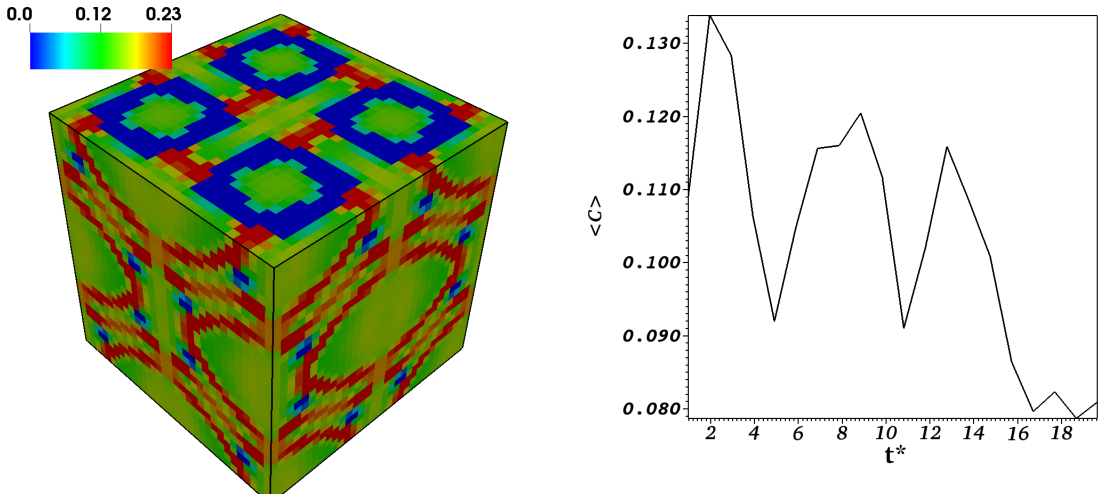


Figure 8: The Smagorinsky constant $C$ estimated at $t^* \approx 3$ (left) and its volume averaged evolution (right) for the DSMA for the resolution of $32^3$ cells.

the transition phase, though in this resolution the difference was smaller. Similarly, the CSMA has performed better during the transition phase but the steeper slope in the dissipation rates during the decay phase denotes overestimated dissipation.

To further analyse the behaviour of the DSMA, the left plot of Fig. 8 shows the instantaneous estimation of the constant $C$ over the domain for the lowest resolution at $t^* \approx 3$. Around this moment, the transition to turbulence is initiated. This is also the time when DSMA started to diverge from the other models. It is evident from the plot that the model was able to identify the inviscid large vortices, the square blue regions with a value close to zero, while a value around 0.1 was estimated in the majority of the domain. However, the constant $C$ reached the maximum available value of 0.23 in regions where the vortices interacted. In an attempt to further examine this issue, the same simulation was rerun without trimming the maximum value. The outcome was regions with overestimated values of $C$, even above 1, indicating that the trimming is necessary. This behaviour is the result of calculating $C$, Eq. (7), locally and not averaging in homogeneous directions, which are all three in this case. This approximation tends to lead to local maxima [11]. However, a complicated and rather expensive algorithm would be needed to identify the homogeneous directions in a real engineering application and is thus avoided. Finally, the right plot in Fig. 8 presents the evolution of the volume averaged values of $C$. The maximum peak is located during the first inviscid part and it is around 35% higher than the value for CSMA, explaining the more dissipative behaviour during this phase. Afterwards, as the time passes its value was reduced, as it is anticipated, due to the gradual depletion of the kinetic energy. During the final phase of decay, it reached values below the one of CSMA ($C = 0.1$) leading to the smoother shape of the dissipation rates.

## 6 CONCLUSIONS

In this paper, we present an easily to implement methodology to verify and evaluate LBM-LES models under wall-free circumstances. To achieve this, initially, we employed the test case of FHIT. For its realisation, the force scheme of [7] was applied, having the important advantage that no initialisation of the velocity field is needed. The disadvantage of this force is the appearance of a resolution-dependent $Re_\lambda$. To deal with this issue, one can still compare the energy spectra of different resolutions by applying suitable non-dimensionalisation [14]. Moreover, having a solution of FHIT case, it is trivial to run DHIT by deactivating the external force. In this way, one can compare different resolutions with the same $Re_\lambda$, by using the same initial data and appropriately locally volume-average them. In the end, the test case of TGV can challenge the models for the situation of an inviscid flowfield transitioning to turbulence and final decay.

By applying the above procedure, we have verified the two newly implemented models, DSMA and WALE. In the case of FHIT and DHIT, we have examined their performance to deal with a fully developed turbulent field showing an expected behaviour. We present that under a reasonably well-resolved mesh, they could be deactivated. On the other hand, in an under-resolved simulation, they estimated a more depleted dissipation range compared to DNS, improving the stability. In comparison with the CSMA, the WALE had identical behaviour while the DSMA seemed to be slightly more dissipative. In the case of DHIT, they managed to capture accurately the large scales of a DNS of higher resolution. Finally, by running the TGV case, we show that both of them tend to overestimate the eddy viscosity during transition to turbulence. The DSMA had the worst performance, particularly in highly under-resolved meshes. However, they were able to adjust their extra dissipation in the final phase of the decay. As for the DSMA, we conclude that the localisation of the calculation of the constant $C$ leads to local maxima and thus a more dissipative behaviour compared to the other models.

### Acknowledgements

This work was supported by UK Research and Innovation under the grant EP/N509747/1 with project number 1831845. The authors also acknowledge the use of the IRIDIS High-Performance Computing Facility, and associated support services at the University of Southampton.

## REFERENCES

[1] Succi, S. *The Lattice Boltzmann Equation for Fluid Dynamics and Beyond*, OUP Oxford, Oxford, New York, 2001.

[2] Deiterding, R. and Wood, S. L. An adaptive lattice Boltzmann method for predicting wake fields behind wind turbines, in: A. Dillmann, G. Heller, E. Krämer, C. Wagner, C. Breitsamter (Eds.), *New Results in Numerical and Experimental Fluid Mechanics X*, Vol. 132 *of Notes on Numerical Fluid Mechanics and Multidisciplinary Design*, Springer, 2016, pp. 845–857.

[3] Deiterding, R. and Wood, S. L. Predictive wind turbine simulation with an adaptive lattice Boltzmann method for moving boundaries, *J. Phys. Conf. Series* 753 (2016) 082005.

[4] Deiterding, R. and Domingues, M. O. Simulation of the flow around an oscillating cylinder with adaptive lattice Boltzmann methods, *in: P. Ivanyi, B. H. V. Topping, G. Varady (Eds.), Proc. 5th Int. Conf. on Parallel, Distributed, Grid and Cloud Computing for Engineering*, Civil-Comp Press, 2017, p. paper 19.

[5] Feldhusen, K., Deiterding, R. and Wagner, C. A dynamically adaptive lattice Boltzmann method for thermal convection problems, *J. Applied Math. and Computer Science* 26 (2016) 735–747.

[6] Deiterding, R. Block-structured Adaptive Mesh Refinement - Theory, Implementation and Application, *ESAIM: Proceedings* 34 (2011) 97–150.

[7] Abdel Kareem, W., Izawa, S., Xiong, A.-K. and Fukunishi, Y. Lattice Boltzmann simulations of homogeneous isotropic turbulence, *Computers & Mathematics with Applications* 58 (5) (2009) 1055–1061.

[8] Hou, S., Sterling, J., Chen, S. and Doolen, G. D. A lattice Boltzmann subgrid model for high Reynolds number flows, *in: A. T. Lawniczak, R. Kapral (Eds.), Pattern formation and lattice gas automata, Vol.* 6, *Fields Inst Comm*, 1996, pp. 151–166.

[9] Premnath, K. N., Pattison, M. J. and Banerjee, S. Dynamic subgrid scale modeling of turbulent flows using lattice-Boltzmann method, *Physica A: Statistical Mechanics and its Applications* 388 (13) (2009) 2640–2658.

[10] Germano, M., Piomelli, U., Moin, P. and Cabot, W. H. A dynamic subgridscale eddy viscosity model, *Physics of Fluids A: Fluid Dynamics* 3 (7) (1991) 1760–1765.

[11] Lilly, D. K. A proposed modification of the Germano subgridscale closure method, *Physics of Fluids A: Fluid Dynamics* 4 (3) (1992) 633–635.

[12] Nicoud, F. and Ducros, F. Subgrid-scale stress modelling based on the square of the velocity gradient tensor, *Flow, Turbulence and Combustion* 62 (1999) 183–200.

[13] Frigo, M. A fast Fourier transform compiler, *in: ACM Sigplan Notices, Vol.* 34, ACM, 1999, pp. 169–180.

[14] Pope, S. B. *Turbulent flows*, Cambridge University Press, Cambridge; New York, 2000.

[15] Orphee, J., Gungor, A., Sanchez-Rocha, M. and Menon, S. Direct and large-eddy simulation of decaying and forced isotropic turbulence using lattice Boltzmann method, *in: 36th AIAA Fluid Dynamics Conference and Exhibit*, American Institute of Aeronautics and Astronautics, San Francisco, California, 2006.